minerals

MDPI

Article

Composition and Pressure Effects on Partitioning of Ferrous Iron in Iron-Rich Lower Mantle Heterogeneities

Susannah M. Dorfman [1,2,*], Farhang Nabiei [1], Charles-Edouard Boukaré [3], Vitali B. Prakapenka [4], Marco Cantoni [5], James Badro [1,3] and Philippe Gillet [1]

[1] Earth and Planetary Science Laboratory, Institute for Condensed Matter Physics, Swiss Federal Institute of Technology Lausanne, 1015 Lausanne, Switzerland; farhang.nabiei@epfl.ch (F.N.); badro@ipgp.fr (J.B.); philippe.gillet@epfl.ch (P.G.)
[2] Department of Earth and Environmental Sciences, Michigan State University, East Lansing, MI 48824, USA
[3] CNRS, Institut de physique du globe de Paris, Université de Paris, F-75005 Paris, France; charles-edouard.boukare@epfl.ch
[4] Center for Advanced Radiation Sources, University of Chicago, Argonne, IL 60439, USA; prakapenka@cars.uchicago.edu
[5] Interdisciplinary Center for Electron Microscopy, Swiss Federal Institute of Technology Lausanne, 1015 Lausanne, Switzerland; marco.cantoni@epfl.ch
* Correspondence: dorfman3@msu.edu

Abstract: Both seismic observations of dense low shear velocity regions and models of magma ocean crystallization and mantle dynamics support enrichment of iron in Earth's lowermost mantle. Physical properties of iron-rich lower mantle heterogeneities in the modern Earth depend on distribution of iron between coexisting lower mantle phases (Mg,Fe)O magnesiowüstite, (Mg,Fe)SiO_3 bridgmanite, and (Mg,Fe)SiO_3 post-perovskite. The partitioning of iron between these phases was investigated in synthetic ferrous-iron-rich olivine compositions $(Mg_{0.55}Fe_{0.45})_2SiO_4$ and $(Mg_{0.28}Fe_{0.72})_2SiO_4$ at lower mantle conditions ranging from 33–128 GPa and 1900–3000 K in the laser-heated diamond anvil cell. The resulting phase assemblages were characterized by a combination of in situ X-ray diffraction and ex situ transmission electron microscopy. The exchange coefficient between bridgmanite and magnesiowüstite decreases with pressure and bulk Fe# and increases with temperature. Thermodynamic modeling determines that incorporation and partitioning of iron in bridgmanite are explained well by excess volume associated with Mg-Fe exchange. Partitioning results are used to model compositions and densities of mantle phase assemblages as a function of pressure, FeO-content and SiO_2-content. Unlike average mantle compositions, iron-rich compositions in the mantle exhibit negative dependence of density on SiO_2-content at all mantle depths, an important finding for interpretation of deep lower mantle structures.

Keywords: iron partitioning; lower mantle; mantle heterogeneities; laser-heated diamond anvil cell; experimental petrology

Citation: Dorfman, S.M.; Nabiei, F.; Boukaré, C.-E.; Prakapenka, V.B.; Cantoni, M.; Badro, J.; Gillet, P. Composition and Pressure Effects on Partitioning of Ferrous Iron in Iron-Rich Lower Mantle Heterogeneities. *Minerals* **2021**, *11*, 512. https://doi.org/10.3390/min11050512

Academic Editor: Yamirka Rojas-Agramonte

Received: 11 March 2021
Accepted: 6 May 2021
Published: 12 May 2021

1. Introduction

Iron-enrichment has been suggested to explain seismic observations of dense regions in the deep lower mantle such as large low shear velocity provinces (LLSVPs) (e.g., [1]) and ultra-low velocity zones (ULVZs) (e.g., [2,3]). For LLSVPs, the difference in Fe/(Mg + Fe), or Fe#, relative to the surrounding mantle is inferred to be as much as 7% based on estimated chemical density differences up to 2% [4]. ULVZs may be more dramatically enriched in Fe to generate density differences of 10% or more. The origin of these regions is unknown, but possibilities include segregation of dense material in a basal magma ocean beneath the crystallizing early mantle [5], accumulation of dense material from subducted slabs [6], or partial melt due to less refractory composition and/or high local temperatures [7]. Understanding these geophysical observations requires dependence of physical properties

such as elasticity, rheology, and electrical and thermal conductivities on composition. The distribution of elements in minerals in the modern mantle is moderated by subsolidus chemical partitioning.

Iron in Earth's lower mantle is distributed between (Mg,Fe,Al)(Fe,Al,Si)O_3 bridgmanite (Bdg), its polymorph (Mg,Fe,Al)(Fe,Al,Si)O_3 post-perovskite (pPv), and (Mg,Fe)O ferropericlase—magnesiowüstite (Mws). Partitioning of Fe between these phases is characterized by the exchange coefficient, K_D, between coexisting silicate and oxide, related to their compositions, X, in equilibrium, where values less than one indicate that iron favors the oxide, and values greater than one the reverse:

$$K_D = \left(X_{Fe}^{Silicate} / X_{Mg}^{Silicate}\right) / \left(X_{Fe}^{Mws} / X_{Mg}^{Mws}\right), \quad (1)$$

This exchange coefficient is used to describe the amounts of Fe in silicate vs. oxide for variable bulk compositions corresponding to hypothesized mantle rocks. Previous experiments have explored silicate-oxide partitioning behavior primarily using San Carlos olivine and pyrolite compositions as analogues for the mantle [8–15]. Due to challenges entailed in modeling iron, computational studies using density functional theory have only recently begun to address partitioning in the lower mantle [16,17]. Previous studies have converged around K_D of ~0.2 to 0.3 in San Carlos olivine near 660 km depth, but substantially higher in pyrolite. The higher K_D in pyrolite is due to incorporation of Al and ferric iron in Bdg [18]. In ferrous-iron-bearing olivine compositions, K_D decreases or remains constant with pressure and increases with temperature and oxygen fugacity.

The dependence of the exchange coefficient on bulk iron content is key to the modern composition of dense mantle heterogeneities. Studies of silicate-oxide iron partitioning in iron-rich compositions with Fe#>16 have found that the exchange coefficient decreases with increasing amounts of ferrous iron, but these studies have been limited to <50 GPa (e.g., [10]). Effects of ferrous iron enrichment on partitioning have been examined to deep lower mantle conditions only along experimental thermal gradients [13] or in relatively iron-poor compositions [11,12,14]. However, partitioning in lower mantle minerals may change at pressures >50 GPa and high ferrous iron content due to composition-dependent structural and electronic changes in bridgmanite.

At the boundary between the transition zone and lower mantle, bridgmanite is stable with no more than 12 mol% $FeSiO_3$, but in the deep lower mantle the solubility limit increases to at least 75% $FeSiO_3$ (e.g., [19]). An increase in solubility may be linked to structural distortion in Bdg and corresponding bonding changes for ferrous iron predicted by density functional theory [20] and confirmed by X-ray diffraction of single crystals [21]. The increase in solubility of iron in Bdg in the deep mantle may also be due to composition-dependence of a high-to-low electronic spin transition in ferrous iron [22]. Since the discovery of pressure-induced spin transitions in ferropericlase [23] and bridgmanite [24], these electronic changes have been explored for their potential effects on partitioning (e.g., [8]) as well as other mantle properties. Differences in Fe-content and $Fe^{3+}/\Sigma Fe$ control the conditions at which spin transitions and partitioning changes occur in the mantle [25,26]. In San Carlos olivine, low $Fe^{3+}/\Sigma Fe$ promotes ferrous iron in Mws, which will undergo a high-to-low spin transition, and Fe^{2+} in Bdg would be predicted to remain in the high-spin state throughout the lower mantle pressure range [20]. However, in more iron-rich compositions, recent studies have suggested that the spin transition in Fe^{2+} in Bdg may occur at ~70 GPa, in the middle of the lower mantle [22,27].

At conditions corresponding to the base of the lower mantle, post-perovskite has also been observed to incorporate at least 80% $FeSiO_3$ [28]. Most studies found that Fe-rich pPv is stable at lower pressures than Fe-poor pPv, e.g., [19,28], suggesting that iron prefers pPv to Bdg. Partitioning of iron from Bdg into pPv is supported by observations of higher K_D for pPv-Mws than for Bdg-Mws when olivine is used as a starting material (e.g., [8]). Conversely, diffraction and microscopy studies of coexisting Bdg and pPv have observed the reverse in pyrolitic starting materials: a preference of iron for Bdg over pPv [29,30]. The conflict between these studies has been attributed to differences in oxidation state

of iron. Partitioning of iron in bridgmanite and post-perovskite at these higher pressures determines whether Fe-enriched silicate phases can explain dense heterogeneities in a potentially SiO_2-rich deep lower mantle (e.g., [2]).

Constraints on chemistry at extreme conditions are best obtained by a combination of in situ phase identification and ex situ composition measurements. In situ X-ray diffraction (XRD) is required to determine the high-pressure phase assemblage, as mantle silicates including Fe-rich Bdg and pPv become amorphous upon quench to ambient conditions. Compositions of all phases can be measured to percent-level under best conditions using a combination of focused ion beam (FIB) and analytical transmission electron microscopy (TEM). The FIB allows extraction and polishing of samples synthesized in the diamond anvil cell for nm-scale compositional measurements in the TEM. In this study, we apply XRD, FIB, and TEM techniques to the partitioning of Fe in Fe-rich mantle phase assemblages synthesized in the laser-heated diamond anvil cell at deep lower mantle conditions. The results are combined with self-consistent thermodynamic modeling to predict physical properties of Fe-rich heterogeneities in Earth's mantle.

2. Materials and Methods

Synthetic fayalite-rich olivines with compositions $(Mg_{0.55}Fe_{0.45})_2SiO_4$ (Fa45) and $(Mg_{0.28}Fe_{0.72})_2SiO_4$ (Fa72) were used as starting materials. Olivines were synthesized from stoichometric mixtures of MgO, SiO_2, FeO, and a small amount of Fe_2O_3 to compensate for nonstoichiometry in FeO. Oxide powder mixtures were reacted in a reducing graphite capsule in a piston-cylinder press (IPGP, Paris) at 1 GPa and 1200 °C for 15 h to produce ~300 μm olivine crystals. Olivine compositions were determined with the JEOL 8200 Superprobe at the University of Lausanne (Table S1), and are consistent with all Fe^{2+} in the starting materials. An additional Fa50 sample synthesized with ^{57}Fe under similarly reducing conditions exhibited 100% Fe^{2+} based on Mössbauer spectroscopy (Supplementary Figure S1).

Single olivine crystals were crushed into 3–10 μm-thick platelets and sandwiched between insulating platelets of NaCl or MgO (the latter medium used for 1 sample which is presented for comparison but not used in partitioning analysis). Materials were dried in a 120 °C oven overnight to remove moisture before loading. Sample assemblages were loaded in symmetric diamond anvil cells with 300 μm-diameter flat anvil culets or 100–150 μm-diameter beveled anvil culets. Gaskets were Re sheets indented to ~25 μm thickness.

Samples were compressed to 33–128 GPa in the diamond anvil cell and laser-heated from both sides to 1900–3000 K. Pressures were determined at 300 K from the diamond anvil Raman peak at the sample position [31] or the equation of state of the NaCl medium [32] before heating. Pressures measured after heating differed from before heating by up to ~2 GPa due to transformation and annealing of the sample and medium. Reported uncertainty for these pressure scales is ~1% under quasihydrostatic loading below 1 Mbar [31], and nonhydrostatic stresses and relaxation may increase uncertainty in pressure to ~3 to 5% [32]. Laser heating was performed for 15–60 min at beamline 13-ID-D of the GSECARS sector of the Advanced Photon Source or at the Earth and Planetary Science Laboratory at Ecole polytechnique fédérale de Lausanne (EPFL). The laser heating system at GSECARS provides a flat-top beam profile for minimal temperature gradients at the sample center [33] and was co-aligned with the ~3 to 4 micron focused synchrotron X-ray beam (0.3344 Å) by visually observing X-ray-induced fluorescence on each sample. The MAR-CCD imaging detector was used to record high-resolution X-ray diffraction in situ at high-pressure and high-temperature conditions. In situ X-ray diffraction is not available during experiments at EPFL. The EPFL system uses a single 1070 nm wavelength, 200 W fiber laser in Gaussian mode divided for double-sided heating using a polarizing beamsplitter. The two sides are independently controlled with rotating wave-plates and focused with 60 mm achromatic lenses. For both GSECARS and EPFL systems the hot spot has a diameter of ~20 μm. Based on tests of the flat-top optics [33], the large (defocused) Gaussian beam spot will produce a similar temperature distribution in the heating spot center as a flat-top spot. Temperature

was determined throughout heating by spectroradiometry over 620–900 nm spectral range. For each sample, a single spot was heated (no scanning of the laser across the sample), and quenched directly from lower mantle temperature conditions by zeroing the laser power.

Chemical analyses of the quench products of these experiments were obtained by electron microscopy. After recovery to ambient conditions, each sample was prepared for ex situ imaging and sectioning. The NaCl medium was dissolved from the surface of each silicate sample with a droplet of deionized water. Each sample was then coated with 10–20 nm of carbon. Heated spots were identified by color (black and opaque vs. transparent unheated olivine) and radially-symmetric topography. Although the diameter of the entire laser-heated area is ~20 μm, the diameter of the hottest part of the sample is ~4 μm (Supplementary Figures S2 and S3). The hottest region exhibits voids at grain boundaries, due possibly to water or release of strain, and larger grain sizes and higher modal abundance of bridgmanite relative to cooler regions.

Thin sections of each heated spot were extracted and polished to electron transparency using a Zeiss NVision 40 (Carl Zeiss AG, Oberkochen, Germany) dual-beam scanning electron microscope and focused Ga^+ ion beam. To prevent damage by the ion beam, a protective layer of carbon 1–2 μm thick was deposited over a ~2 × 20 μm^2 area across the center of each heating spot. Additional carbon patches were deposited to support particularly thin (~1 μm-thick samples recovered from ~1 Mbar pressure) or fragile samples (with cracks or holes). Slices were milled to 1–2 μm thick at 30 kV and 1.5–27 nA before transfer to TEM grid. The center of each slice was then polished to 100–200 nm thickness at 30 kV and 300 pA. Final cleaning and polishing was performed at 5 kV and 80 pA at a 5° angle to the surface. As in previous work [8], a few slices were lost during the lift-out procedure.

Sections were transferred to a FEI Tecnai Osiris analytical TEM for composition analysis. Accelerating voltage for these measurements was 200 kV. To avoid selective migration of elements from measurement spots [34], chemical measurements were obtained in scanning mode from maps. EDX maps were acquired at 10,000–50,000 (typically ~40,000) counts/second with pixel dwell time of 50 microseconds scanned over 1024 × 1024 pixels for total scanning time ~10 min. Compositions of individual grains were summed over selected ~100 nm regions within maps. In the hot spot centers, two samples had grain sizes smaller than the 100–200 nm thickness of the polished thin section and due to grain overlap were not suitable for composition analysis. Grain sizes decreased significantly at higher pressures, requiring longer heating times. We evaluated the quality of chemical measurements and magnitude of potential Soret diffusion [35] from the Si-content measured in oxide grains due to overlap with silicate grains. All measurements included in this study have less than 4% Si/(Mg + Fe + Si) measured in magnesiowüstite. Compositions measured for samples obtained via EDX are listed in Table 1 and Supplementary Table S2. Reported uncertainties are standard deviations of composition measurements for selected grains used for composition measurements in each sample. Measurements of unheated olivine regions of samples agree with compositions measured by microprobe to 1–2%, supporting accuracy of EDX.

Table 1. Composition measurements by XRD and EDX and corresponding experimental conditions pressure (P), temperature (T), and duration (t). K_D is defined as $\left(X_{Fe}^{Silicate}/X_{Mg}^{Silicate}\right)/\left(X_{Fe}^{Mws}/X_{Mg}^{Mws}\right)$, where X is concentration of the subscript element in the superscript phase. Uncertainties are taken from statistical error in EDX quantification. * = Laser heating and X-ray diffraction conducted at APS beamline 13-ID-D. Missing data: NR = Lattice parameters not resolvable from diffraction data, NA = No diffraction available, TS = grain sizes too small for EDX measurements. Phases: Bdg = bridgmanite, pPv = post-perovskite, Mws = magnesiowüstite, and Sti = stishovite.

Sample	P (GPa)	T (K)	t (min)	Phases	X_{Fe}^{Bdg} (XRD)	X_{Fe}^{Bdg}	X_{Fe}^{Mws}	K_D
Fa45 *	40	2000	10	Mws, Bdg, Sti (1 grain)	25 ± 5	17.9 ± 1.9	74.7 ± 1.8	0.074 ± 0.018
Fa45 *	46	2050	20	Mws, Bdg	14 ± 5			Recovery failed
Fa45 *	62	2000	15	Mws, Bdg	27 ± 5	16 ± 3	73.6 ± 1.1	0.07 ± 0.03
Fa45 *	66	2250	15	Mws, Bdg	21 ± 5			Recovery failed

Table 1. *Cont.*

Sample	P (GPa)	T (K)	t (min)	Phases	X_{Fe}^{Bdg} (XRD)	X_{Fe}^{Bdg}	X_{Fe}^{Mws}	K_D
Fa45 *	71	2440	20	Mws, Bdg	18 ± 5		TS	-
Fa45 *	89	2600	15	Mws, Bdg	4 ± 5	18 ± 4	64 ± 2	0.12 ± 0.05
Fa72 *	33	1980	15	Mws, Bdg, Sti	56 ± 5	37 ± 3	86.8 ± 0.3	0.089 ± 0.016
Fa72	39	2000	30	Mws, Bdg, Sti	69 ±5	47 ± 7	92.4 ± 1.2	0.07 ± 0.04
Fa72 *	48	1900	15	Mws, Bdg	NR	43 ± 5	92.2 ± 0.6	0.06 ± 0.02
Fa72	52	2000	30	Mws, Bdg	NA	46.5 ± 1.3	95.3 ± 0.8	0.043 ± 0.011
Fa72 *	61	1850	20	Mws, Bdg	55 ± 5		TS	-
Fa72	82	2000	20	Mws, Bdg, Fe	NA	51 ± 2	98.2 ± 0.5	0.019 ± 0.009
Fa72 *	89	2200	35	Mws, Bdg, pPv	31 ± 5	49 ± 2	96.8 ± 1.1	0.032 ± 0.014
Fa72	128	2700	60	Mw, pPv	NA	pPv: 59.1 ± 0.8	97 ± 3	0.05 ± 0.07
Fa72 in MgO	83	2200	45	Fp, Mws, Bdg	NA	4.2 ± 0.7	21.9 ± 0.9, 96.4 ± 0.5	-

3. Results

3.1. Phase Identification

Phases and compositions were identified ex situ for all experiments as well as in situ for experiments conducted at GSECARS with X-ray diffraction. Diffraction patterns recorded at heating spot centers after temperature quench exhibited peaks corresponding to bridgmanite, magnesiowüstite, stishovite, and a single peak attributed to $CaIrO_3$-type post-perovskite (Figure 1, Supplementary Figure S4). In the Fa45 composition from 40 to 89 GPa (all pressures studied with X-ray diffraction), all observed diffraction peaks match Bdg or Mws (Supplementary Figure S4). In Fa72 at 33 GPa, corresponding to the shallow lower mantle, stishovite is also observed (Figure 1). The exsolution of stishovite indicates that bridgmanite cannot accommodate all available iron and breaks down to a mixture of bridgmanite, stishovite, and magnesiowüstite. At higher pressures, the solubility of Fe in Bdg increases [19,29,36], and the stishovite phase disappears. Identification of stishovite and magnesiowüstite by EDX in recovered samples concurs with observations by X-ray diffraction. Pure SiO_2 regions were identified in composition maps of samples synthesized at and below 40 GPa, but not in samples synthesized at higher pressures (Figure 2, Table 1).

Although Fe metal droplets have been observed in multiple previous studies of lower mantle phase assemblages (e.g., [8,37]), they were not typically present in samples analyzed in this work. Metallic iron is detectable in recovered samples as oxygen-depleted regions in EDX maps. In one sample Fe metal droplets ~10 to 50 nm were embedded in a large grain of nearly pure FeO (Supplementary Figure S5). Unlike these droplets, Fe-rich inclusions in Bdg grains were not typically depleted in oxygen (Supplementary Figure S6). In contrast to previous experiments on less Fe-rich compositions, we do not observe Fe metal grains within Bdg due to disproportionation. This lack of metallic Fe is evidence that iron remains ferrous after synthesis of the lower mantle phase assemblage.

Silicates bridgmanite and post-perovskite in recovered samples could not be distinguished due to amorphization. With one exception, Bdg was amorphous (e.g., Supplementary Figure S7); Bdg with high Fe-content (Fe# $\geq$ 38) is not quenchable [19]. The amorphous silicate is the interconnected phase, as Bdg has been in previous studies [8]. Iron-depleted Fe#4 Bdg in the sample loaded in MgO (final sample listed in Table 1) was successfully quenched, and crystalline Bdg was observed before composition mapping. Bridgmanite lattice planes subsequently disappeared after composition mapping due to damage by the electron beam. Crystalline $(Mg,Fe)SiO_3$ pPv is also not quenchable to ambient conditions, and we were thus unable to conclusively identify a pPv phase in recovered samples. A single amorphous silicate phase quenched from synthesis at 128 GPa is assumed to have been post-perovskite.

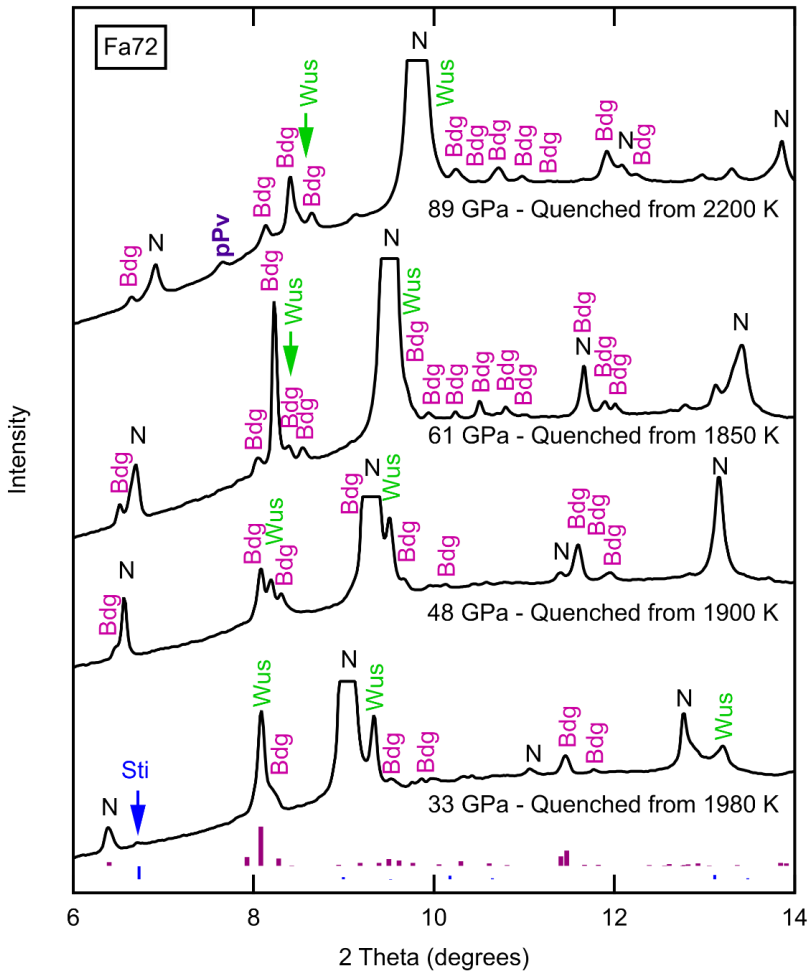

Figure 1. Diffraction patterns for phase assemblages synthesized from Fa72 at 33–89 GPa. Bdg = bridgmanite, pPv = post-perovskite, Wus = wüstite/magnesiowüstite, Sti = stishovite, N = NaCl medium. Due to overlap between oxide and NaCl peaks, we cannot resolve whether the structure is B1 cubic or rhombohedral, though EDX results indicate 92–98% FeO. Reference stick patterns for Bdg and Sti are provided below. For these experiments, λ = 0.3344 Å.

3.2. Compositions of Coexisting Phases and Partitioning

The compositions determined from EDX mapping for bridgmanite and magnesiowüstite are listed in Table 1 and Supplementary Table S2. Listed uncertainties in measured compositions and partitioning coefficients were obtained from a standard deviation of compositions of multiple grains at the sample center, and may be an underestimate due to sample topography and matrix effects. The total Fe# of the phase assemblage in the center of the heating spot is ±3 Fe# of the starting materials (note that for phase assemblages that include substantial stishovite, the bulk Fe# is not the average Fe# of Bdg and Mws, but an average over the entire measured region), confirming that the sample center did not lose or gain a significant amount Fe by Soret diffusion [35]. The outer portion of the laser heating spot, where thermal gradient was significant, does exhibit compositional differences due to Soret diffusion, and data from these regions were not used in further analysis. Due to reaction between the sample and the MgO medium, the sample with the MgO medium is not included in further analysis of compositions and partitioning. Bridgmanite compositions are Fe#16–18 for Fa45 and Fe#37–51 for Fa72 (Figure 3a). Measured compositions of Bdg formed from Fa72 are slightly more Fe-rich than the maximum solubility of $FeSiO_3$ in Bdg measured at ~2000 K in multianvil press experiments to 50 GPa [36] (Figure 3b). The consistently higher maximum Fe-content in Bdg in these experiments relative to Tange et al. [36] may be due to underestimation of temperature during laser

heating, overestimation of Fe-content by EDX, or other experimental differences in run time and/or redox state. Magnesiowüstites formed from Fe-rich olivines are extremely Fe-rich: Fe#64–75 in Fa45 samples and Fe#87–98 in Fa72 (Figure 3b). Compositions measured by EDX for Bdg and Mws determine values for K_D that are lower than previous studies of less Fe-rich San Carlos olivine, decrease with pressure, and increase with temperature (Figure 4). This is consistent with previous observations at lower pressures of stronger preference of ferrous iron for Mws in Fe-enriched bulk compositions (e.g., [10,36]). The exchange coefficient decreases with pressure for the Fa72 composition. While partitioning appears flat with increasing pressure in the Fa45 composition, this is likely an effect of higher temperatures during the higher pressure runs for this composition, and we may expect the exchange coefficient to decrease with pressure at a constant temperature. Post-perovskite at 128 GPa was measured to have Fe#59, higher than any Fe# measured for bridgmanite. This results in a higher post-perovskite—magnesiowüstite exchange coefficient relative to bridgmanite—magnesiowüstite (Figure 4), in agreement with previous studies of San Carlos olivine by Auzende et al. [8] and Sakai et al. [11].

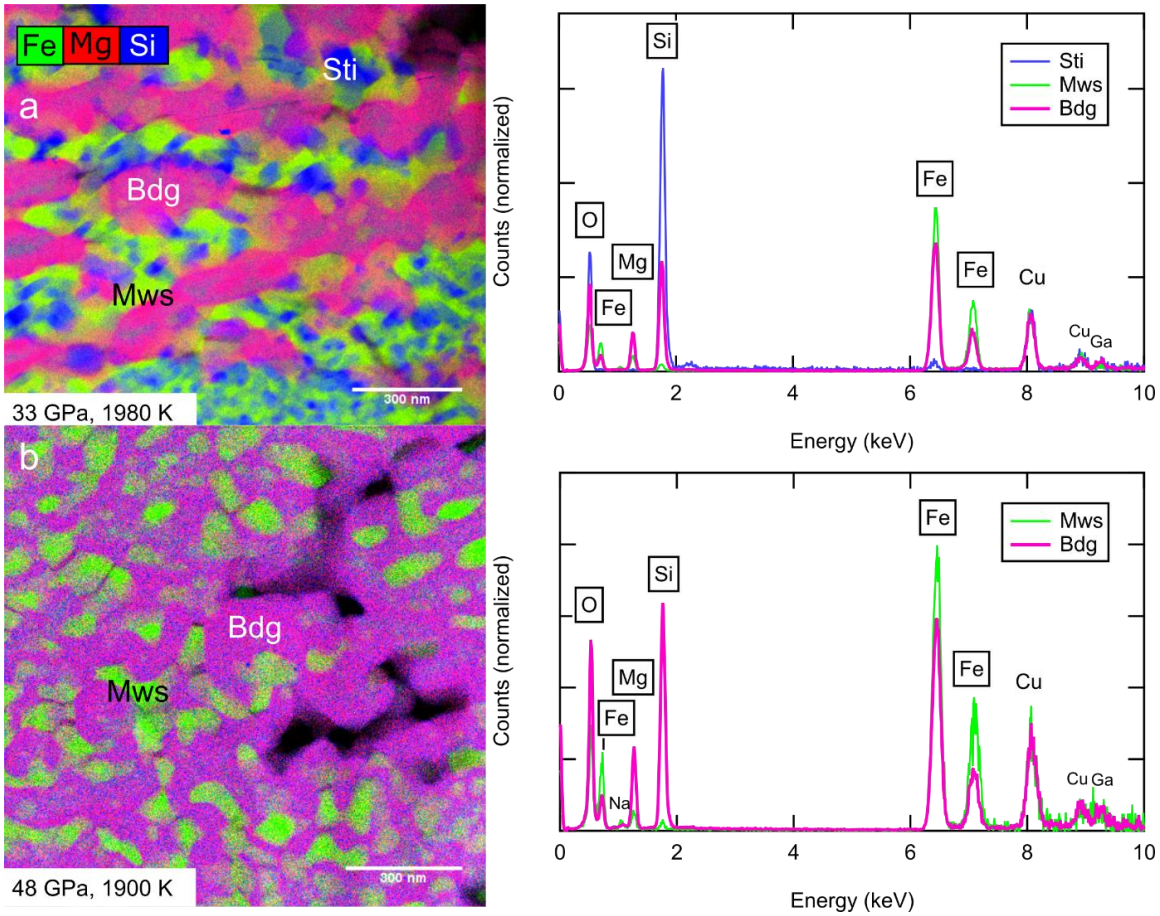

Figure 2. Energy-dispersive X-ray maps with Mg, Fe, and Si concentrations in red, green, and blue, respectively, and corresponding spectra obtained from selected grains for (**a**) Fa72 heated to 1980 K at 33 GPa and (**b**) Fa72 from 48 GPa. Bdg = bridgmanite, Mws = magnesiowüstite, Sti = stishovite. Cu signal is from the TEM grid, and minor Ga remains from ion milling.

Lattice spacings of bridgmanite, magnesiowüstite and post-perovskite, when resolvable, also provide estimates of the partitioning of iron. This analysis has previously been attempted for high-pressure diffraction data [38], but more recent studies offer improved constraints on the equation of state of lower mantle phases, including effects of iron on the compressibility of bridgmanite and effects of the spin transition on ferropericlase. Lattice parameters of Bdg in olivine compositions in this work at pressures determined by the

NaCl medium are consistent with Fe#0–20 in Fa45 and Fe#40–70 in Fa72 (for more details see Appendix A, Supplementary Figure S8; Table 1). These values are consistent with EDX observations (Supplementary Figure S8) to ~20 Fe#. At all pressures, observed unit cell volumes for magnesiowüstite support Fe-enrichment relative to the starting composition (Supplementary Figure S9), also consistent with EDX observations (Figure 3b).

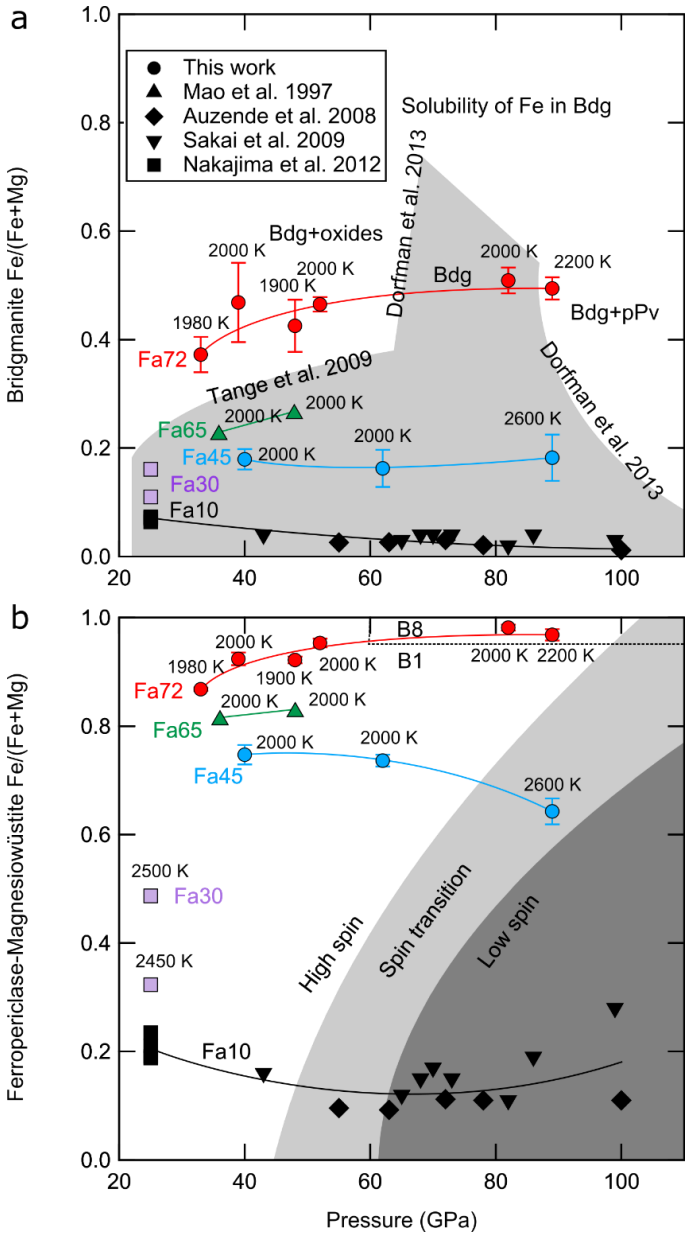

Figure 3. Composition data obtained from partitioning studies in olivine compositions plotted with relevant phase stability data. Data from this study and those from Auzende et al. [8] and Nakajima et al. [10] were obtained by EDX in the TEM. Data from Mao et al. [39] are based on X-ray diffraction at ambient conditions. (**a**) Compositions for bridgmanite synthesized from olivine starting materials. Gray shaded region marks solubility of Fe in bridgmanite at ~2000 K from previous studies in the multianvil press [36] and laser-heated diamond anvil cell [19]. (**b**) Compositions of (Mg,Fe)O synthesized from olivine starting materials. Shaded regions show change in the pressure of the high-to-low spin transition with composition [40,41]. The rectangle indicates the pressure/composition range of previous observations of B8 FeO [42,43]. Although two of our data indicate Fe/(Mg+Fe) for (Mg,Fe)O and synthesis conditions that could correspond to B8 structure, our XRD observations could not confirm a structural difference during or after heating.

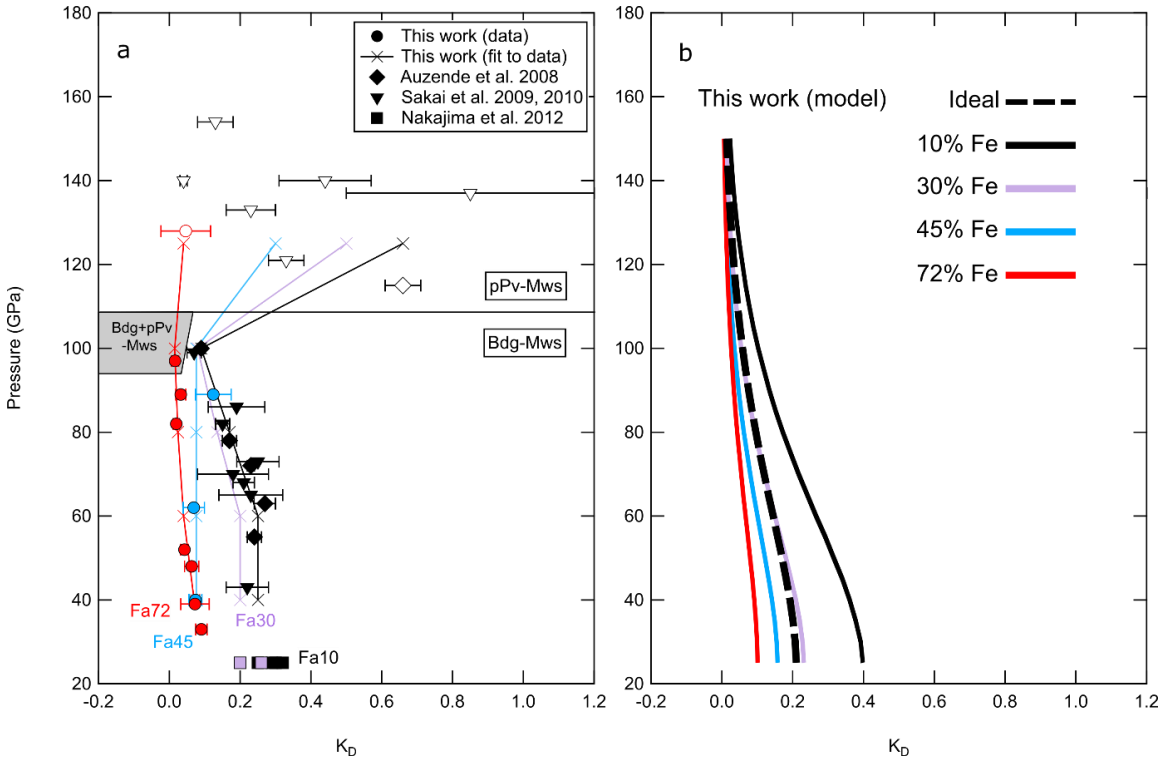

Figure 4. (**a**) Exchange coefficient between silicate and oxide phases at lower mantle conditions from experiments in this and previous studies [8,10–12] compared to thermodynamic models. Filled/open symbols indicate a bridgmanite/post-perovskite silicate phase. For most data, temperatures were in the range 1850–2200 K (temperatures for all data in this study listed in Table 1). Light gray region indicates composition/pressure space with coexisting bridgmanite and post-perovskite. Values chosen for fit to compositions Fa10, Fa30, Fa45, and Fa72 at selected pressures 40, 60, 80, 100, and 125 GPa are shown in 'x' symbols and lines. (**b**) Modeled pressure- and composition-dependence of partitioning behavior between bridgmanite and ferropericlase in olivine bulk compositions assuming ideal mixing (black dashed curve) and nonideal mixing (solid curves) using updated thermodynamic parameters based on thermal equation of state of FeO by [42] and inversion of experimental partitioning data in this study.

At 89 GPa in Fa72, lattice parameters of bridgmanite indicate only Fe# ~30, likely due to partitioning of Fe into incipient pPv. The most prominent diffraction line of pPv, (022) is observed in this diffraction pattern. The lattice spacing indicated by this peak is large relative to that observed for Fe#40 pPv at similar pressures, supporting very high Fe-content [44]. The initiation of the post-perovskite transition at only 89 GPa is compatible with the shallow, broad post-perovskite transition in Fe-rich (Mg, Fe)SiO_3 observed in previous studies [2,19,28].

3.3. Thermodynamic Modeling

Variation of partitioning behavior as a function of bulk iron content in the olivine system implies non-ideal mixing behavior. To determine the thermodynamic properties consistent with observed partitioning behavior, we carried out thermodynamic modeling of partitioning in olivine bulk compositions at lower mantle conditions. Iron partitioning between Mws and Bdg when SiO_2 stishovite is not present refers to the following chemical reaction,

$$MgSiO_3 + FeO \leftrightarrow FeSiO_3 + MgO, \quad (2)$$

which can be rewritten in terms of chemical potential,

$$\mu MgSiO_3 + \mu_{FeO} \leftrightarrow \mu FeSiO_3 + \mu_{MgO} \quad (3)$$

where μ_i is the Gibbs free energy of species i. The chemical potential will vary as a function of temperature:

$$\mu_i = \mu_i^0 + RT\log(x_i\gamma_i), \quad (4)$$

where x_i and γ_i are the mole fraction and coefficient of activity of species i, respectively. We assume that mixing is ideal in the Bdg phase (i.e., $\gamma_{MgSiO_3} = \gamma_{FeSiO_3}$). However, non-ideal mixing has been documented in the Mws phase [45], and can be described by a Margules interaction parameter W.

$$RT\log(\gamma_{MgO}) = W(1 - x_{MgO}), \quad (5)$$
$$RT\log(\gamma_{FeO}) = W(1 - x_{FeO}),$$

Using Equations (1)–(5), we obtain

$$RT\log(K_D) = \mu^0_{MgSiO_3} - \mu^0_{FeSiO_3} + \mu^0_{MgO} - \mu^0_{FeO} - W(2x_{FeO} - 1), \quad (6)$$

In Equation (6), x_{FeO} is constrained by the bulk Fe/(Fe + Mg) ratio of the system and the relative amount of Mws relative to Bdg,

$$x_{FeO}(1 - Y) + x_{FeSiO_3}Y = Z, \quad (7)$$

where Y is the relative proportion of Bdg (i.e., Bdg/(Bdg+Mws) and Z is the bulk Fe/(Fe + Mg) ratio of the system. It should be noted that in the ideal mixing case (i.e., W = 0), K_D is insensitive to the bulk iron content of the system that controls x_{FeO}; as the experimental observations described above demonstrate a dependence of K_D with bulk iron content, non-ideality in either the Mws or Bdg phase is required to describe iron partitioning in iron-rich olivine systems.

Thermodynamic parameters for Mws and Bdg phases have been constrained by previous studies, for example summarized in a database by [46]. The equation of state of iron-bearing Bdg and free energies consistent with observed phase equilibria in the $MgSiO_3$-$FeSiO_3$ sytem were updated by [47]. However, an initial attempt to model iron partitioning between Mws and Bdg according to the above framework yielded K_D inconsistent with experimental observations (Supplementary Figure S10). While experimental data indicate K_D decreasing with pressure, the modeled K_D increases with pressure for all compositions.

To correct this discrepancy, we first updated the equation of state parameters for FeO using the values from [42]. Next, we adjusted the reference chemical potential (F_0 in the [46] thermodynamic database) to fit the mean value of K_D at 40 GPa. These changes produce a reasonable pressure-dependence for K_D (Figure 4b) self-consistently using Equation (6), whether mixing in the Mws system is assumed to be ideal or non-ideal. The interaction parameter W is then inverted from the experimental data presented in this study (Figure 4) using the forward model for K_D in Equation (6). The resulting thermodynamic parameters for FeO are shown in Table 2. This model successfully reproduces the partitioning observations in ferrous-iron-bearing systems in this and previous studies [8,10,12], as well as previous observations of the stability of iron-rich bridgmanite [19] (Figure 5).

Table 2. Thermodynamic parameters for FeO employed in partitioning and phase equilibrium modeling: 1 bar volume V_0, 1 bar bulk modulus K_0, pressure-derivative of the bulk modulus $K_{0'}$, Grüneisen parameter γ_0, second-order Grüneisen parameter q, Debye temperature θ_0, reference chemical potential F_0, and Margules parameter for ferropericlase W. Values for these parameters from [46] were updated per measurements by [42] and further modified to produce partitioning behavior in agreement with experimental data.

	Previous Parameters	Revised Parameters
V_0 (cm^3/mol)	12.26 [a]	12.26
K_0 (GPa)	179 [a]	149 [b]
$K_{0'}$	4.9 [a]	3.6 [b]
γ_0	1.53 [a]	1.53
q	1.7 [a]	1.7
θ_0 (K)	454 [a]	454
F_0 ($\times 10^3$ J/mol)	−242 [a]	−235 [c]
W ($\times 10^3$ J/mol)	13 [a]	14.746 [c]

[a] Ref [46]. [b] Ref [42]. [c] This study.

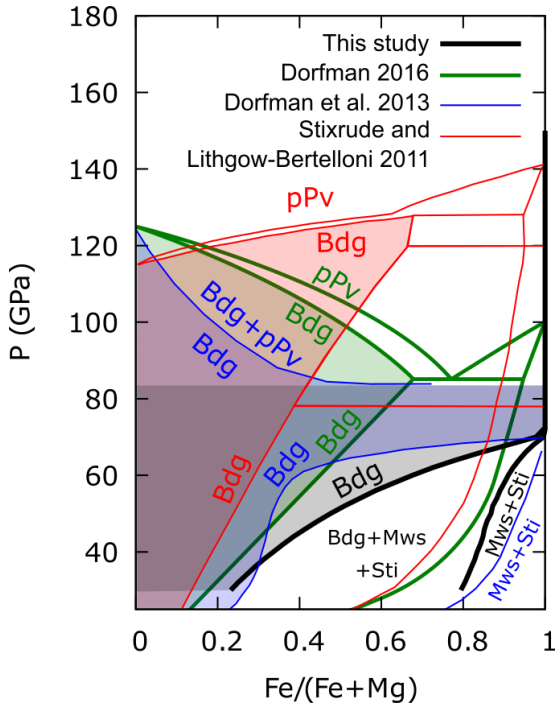

Figure 5. Phase diagram of $MgSiO_3$-$FeSiO_3$ system at ~2000 K based on experimental observations (blue: [19]) and thermodynamic calculations in previous work (red: [46], green: [47]) and this study (bold black lines). Thermodynamic calculations using excess mixing volume term in this study successfully reproduce experimental observations of very high solubility of $FeSiO_3$ in bridgmanite at deep lower mantle pressures >80 GPa. Regions in pressure-composition space where single phase bridgmanite are stable are highlighted for each phase diagram.

4. Discussion

4.1. Multivariable Effects on Partitioning

The experiments presented here examine substantially more Fe^{2+}-rich compositions than those explored in previous studies of partitioning in Earth's deep lower mantle, and thus provide systematic constraints on effects of compositional differences on partitioning in iron-rich heterogeneities. Previous studies have observed two major trends of partitioning with increasing pressure/depth for different compositions [18]: in San Carlos olivine, with no Fe^{3+}, silicate-oxide K_D is flat or decreases between 50 and 100 GPa and increases across the post-perovskite transition [8,11–13,16], while pyrolite, with high $Fe^{3+}/\Sigma Fe$, K_D exhibits a more complex behavior in the Bdg stability field, and decreases across the pPv transition [9,15,48]. Below 50 GPa in other olivines, presumably with low $Fe^{3+}/\Sigma Fe$, K_D decreases with total Fe# [10,36,49], and this work demonstrates that the trend for iron-rich compositions at higher pressures continues to be shifted to lower K_D values relative to San Carlos olivine.

Differences in partitioning behavior between Fe-rich and Fe-poor compositions may be due to differences in the conditions at which high-to-low spin transitions occur in Fe-bearing mantle phases. The decrease in K_D in low $Fe^{3+}/\Sigma Fe$ olivine was linked to the spin transition of Fe^{2+} in magnesiowüstite [23]. In more Fe-rich olivine, any decrease in K_D can be expected to occur at higher pressures due to the increase in high-to-low spin transition pressure with Fe# in magnesiowüstite [40,41]. The spin transition in Fe#~70 magnesiowüstite in Fa45 can be estimated to begin at ~80 GPa based on observations of similar compositions [40,41,50]. The spin transition in FeO does not occur until ~120 GPa, particularly at high temperatures corresponding to conditions during partitioning, e.g., [43] (Figure 3a). We can assume that in Fa72 samples, with magnesiowüstite compositions close to pure FeO, the spin transition does not occur in magnesiowüstite in the bridgmanite stability field. However, a gradual decrease is observed in K_D in Fa72 in this study (Figure 4).

This suggests that at high Fe-contents, a decrease in K_D may arise from pressure effects alone on thermoelastic properties of Bdg and Mws.

Spin transitions in bridgmanite may increase the partition coefficient, but this has been less clear due to multiple possible crystallographic sites and valence states for Fe [26]. Increases in K_D due to spin transitions in Bdg have been proposed due to a high-to-low spin transition in Fe^{3+} at <30 GPa [25]. Since olivine starting materials for these experiments are nominally Fe^{3+}-free, a spin transition in Fe^{3+} will only have a significant effect on K_D if during Bdg/Mws synthesis a substantial amount of Fe^{2+} is oxidized to Fe^{3+}. Oxidization of Fe^{2+} was limited in Bdg and Bdg-Mws mixtures synthesized from ~100% ferrous starting materials under identical loading and heating protocols to experiments in this study, resulting in $Fe^{3+}/\Sigma Fe$ of less than 13–25% [51]. In addition, substantial disproportionation of Fe^{2+} to Fe^{3+} and Fe^0 metal is not supported by TEM observations detailed above. A high-to-low spin transition in Fe^{3+} is thus unlikely to significantly affect partitioning in these experiments. Although a high-to-low spin transition does not occur in Fe^{2+} at mantle-relevant pressures in bridgmanite with low Fe# [20], higher Fe-content may promote this transition in bridgmanite at lower pressures [22,27,52,53]. For Fe#75, a fraction of Fe^{2+} in Bdg may adopt the low spin state by 80 GPa [22]. Although Bdg in Fa72 samples reaches Fe# > 40, this is not sufficiently Fe-rich to promote a spin transition in Fe^{2+}. The lack of effects of any spin transition in bridgmanite on partitioning is consistent with the strictly decreasing trend of K_D in Fa72 in the bridgmanite stability field (Figure 4).

Observations of the partitioning of Fe between bridgmanite and magnesiowüstite versus post-perovskite and magnesiowüstite provide important constraints on the post-perovskite transition in Fe-bearing compositions in the mantle and the D" discontinuity. Most measurements of phase equilibria by X-ray diffraction support a lower-pressure, broader pPv transition in Fe-rich compositions [2,19,28,54], which implies that Fe partitions from Bdg into the pPv phase. Partitioning of Fe from Bdg to pPv is also supported by observations of higher silicate-oxide K_D for pPv than for Bdg [8,11,12]. However, a few studies have suggested that Fe partitions in the opposite direction, based on a higher pPv transition pressure in the presence of Fe [29] and direct partitioning measurements between coexisting silicates [14,30,55]. The conflict has been attributed to differences in the $Fe^{3+}/\Sigma Fe$ content of starting materials and synthesized silicates [14,18,26], which is not well-known for all experiments and challenging to determine both in situ and ex situ. The experiments in this study support a higher K_D for post-perovskite–magnesiowüstite relative to bridgmanite–magnesiowüstite, suggesting a shallower, broader depth for the post-perovskite transition in iron-rich lower mantle heterogeneities.

4.2. Physical Properties of Mantle Heterogeneities

Dense mantle heterogeneities may have formed through the crystallization of a basal magma ocean, subduction of dense material, or a combination of multiple mechanisms. Although some models have proposed that such regions could remain relatively chemically isolated over Earth's history, preserving primordial material rich in incompatible elements (e.g., [56]), depending on the amount of mixing the compositions of heterogeneous regions must be a time-integrated result of chemical behavior during their segregation and since. For example, the basal magma ocean hypothesis may imply that the final dense residue is depleted in Si and enriched in Fe relative to a dominantly bridgmanite lower mantle [5]. The density of large low shear velocity provinces could be consistent with iron-enrichment [56], but whether subducting slabs mix into these regions is not known. To test all models of modern compositions of dense heterogeneities using modern observations of seismic properties, we need to be able to model chemical partitioning between arbitrary mixtures of bridgmanite and oxide phases.

Based on our modeled composition- and pressure dependence of iron partitioning, we obtain compositions and physical properties of the major phases in the deep lower mantle for a heterogeneous lower mantle containing iron-rich regions. We examine compositions with total Fe# 10, 30, 45, and 72 at selected pressures 40, 60, 80, 100, and 125 GPa (corresponding to depths of roughly 1050, 1470, 1870, 2250, and 2700 km, respectively).

Note again that the partitioning values from this work represent low ferric iron and fixed ~peridotitic SiO_2-content. We assume that K_D is independent of mol% SiO_2, expressed as mol% bridgmanite in a bridgmanite–magnesiowüstite phase assemblage.

Model compositions for variable Fe#, mol% SiO_2 and pressure are combined with measurements of physical properties of bridgmanite and magnesiowüstite to determine the observable seismic properties of mantle heterogeneities. Recent experimental equation of state measurements over a wide range of compositions have confirmed that the densities of bridgmanite and post-perovskite vary linearly with Fe^{2+}-content (Supplementary Figure S11) [4]. The Fe#- and pressure-dependence of density of ferropericlase/magnesiowüstite requires a more complex model due to the composition-dependent spin transition. Below the onset of the spin transition, oxide density varies linearly with Fe-content, but at higher pressures the spin transition results in systematically higher densities for ferropericlase relative to FeO. Densities of mantle phase assemblages at lower mantle pressures and room temperature (Figures 6 and 7) were modeled as weighted means between the silicate and oxide densities (see Appendix A). A room-temperature density calculation ignores any difference in thermoelastic properties between Fe-poor and Fe-rich systems, but requires minimal extrapolation from existing experimental data. This model also does not consider Fe^{3+}-rich mantle compositions, in which K_D is substantially different both above and below the post-perovskite transition [26] and a spin transition in bridgmanite affects density (e.g., [57]). Another source of uncertainty in the model is limited experimental constraints on temperature-dependence of partitioning at deep mantle conditions, with 100s K differences in temperature between the experimental data (Figure 4). However, modeled densities are not highly sensitive to uncertainty in partitioning: 50% error bars on K_D result in uncertainty in modeled density of the resulting assemblage of ~0.2 to 1% in the deep mantle.

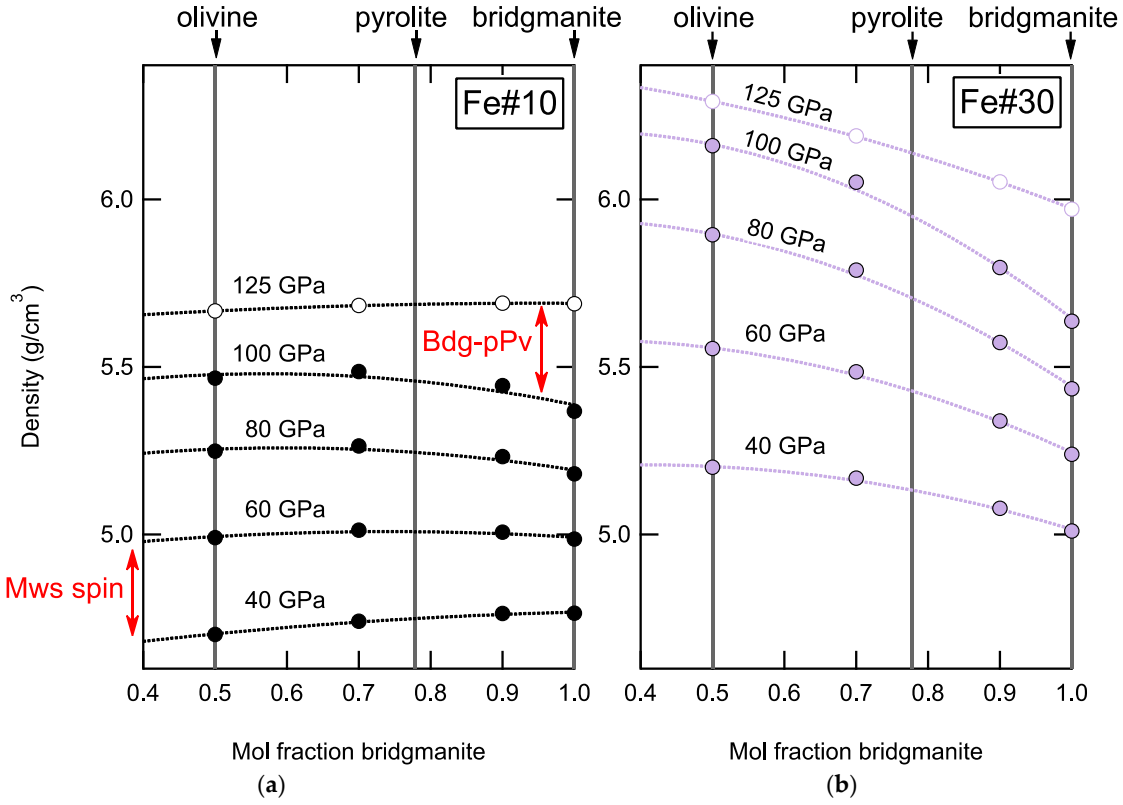

Figure 6. Density of a lower mantle phase assemblage comprising ferrous-iron-bearing bridgmanite, ferropericlase, and post-perovskite as a function of mol% silicate and pressure. The % bridgmanite marked "pyrolite" corresponds to the pyrolite Mg/Si ratio, but does not address other elemental abundances in pyrolite (e.g., Al and Ca). Densities are calculated based on partitioning data in this study and equation of state data for bridgmanite, ferropericlase, and post-perovskite as

detailed in Supporting Text. Filled symbols = bridgmanite and ferropericlase phase assemblage, open symbols = post-perovskite and ferropericlase. Compositions are modeled at pressures 40, 60, 80, 100, and 125 GPa (dotted lines = isobars) for fixed bulk Fe# (**a**) Fe#10, representing average mantle, and (**b**) Fe#30, representing dense mantle heterogeneity.

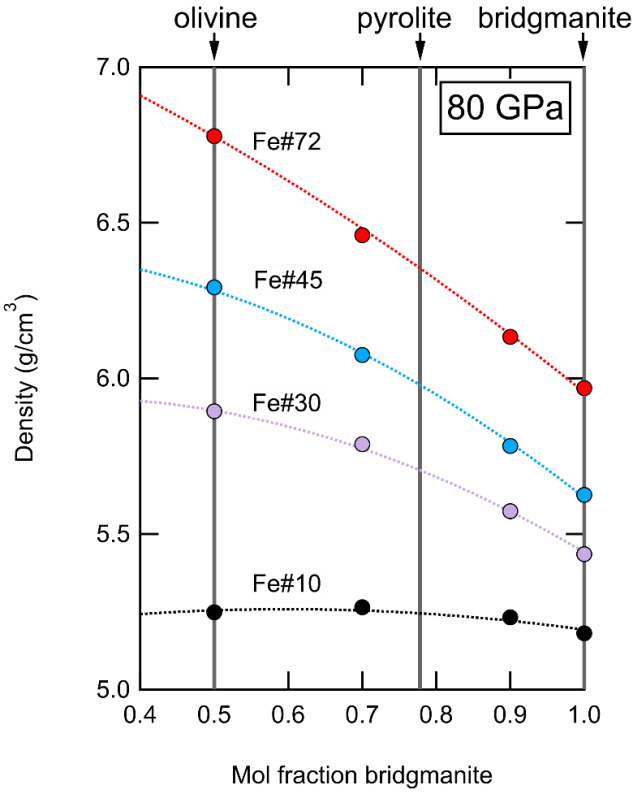

Figure 7. At 80 GPa, modeled densities of lower mantle phase assemblages comprising ferrous-iron-bearing bridgmanite and ferropericlase. Model compositions (symbols) vary in mol% bridgmanite and bulk iron content. The % bridgmanite marked "pyrolite" corresponds to the pyrolite Mg/Si ratio, but does not address other elemental abundances in pyrolite (e.g., Al and Ca). Dotted lines for constant bulk Fe# are provided as guides to the eye.

While it is well-known that increasing Fe# of the mantle phase assemblage increases its density, the effect of variable SiO_2-content on mantle dynamics is perhaps less intuitive. In average lower mantle rock with Fe#10, the change in density due to difference in mol% SiO_2, $\partial\rho/\partial SiO_2$, is nearly zero (Figure 6). Increasing the fraction of bridgmanite in the mantle slightly increases net density in the shallow lower mantle (40 GPa and lower pressures). With increasing pressure, differences in compressibility between bridgmanite and ferropericlase result in a slightly negative change in density with increasing bridgmanite fraction. The post-perovskite transition increases the density of the silicate and $\partial\rho/\partial SiO_2$ becomes slightly positive again at 125 GPa. Adding iron to the mantle not only increases the density, it also modifies $\partial\rho/\partial SiO_2$ (Figures 6 and 7). An Fe#30 dense mantle heterogeneity exhibits negative $\partial\rho/\partial SiO_2$ at all modeled pressures (Figure 6). For very Fe-rich compositions at deep mantle pressures, $\partial\rho/\partial SiO_2$ becomes comparable in magnitude to $\partial\rho/\partial$Fe# (figfig:minerals-1160514-f007). The depth- and composition-dependence of $\partial\rho/\partial SiO_2$ may provide a mechanism for compositional stratification in the mantle, leading to Fe-bearing, Si-depleted LLSVPs, and ULVZs.

Heterogeneous mantle SiO_2-content may also explain enigmatic differences in seismic velocities V_S and V_P in LLSVPs [56]. The deep lower mantle has been noted for anticorrelation of V_S and V_P, which neither thermal differences nor iron content alone can explain [4]. However, differences in Fe-content in combination with SiO_2-content produce complex effects on density and compressibility. Further studies on composition, pressure, and tem-

perature dependence of thermoelastic properties will test whether dense heterogeneities such as LLSVPs are enriched or depleted in SiO_2.

5. Conclusions

In order to systematically investigate the effects of iron enrichment on the properties of dense LLSVPs and ULVZs, partitioning of iron between magnesiowüstite, bridgmanite, and post-perovskite was examined in Fe^{2+}-rich olivine compositions, Fa72 and Fa45, at pressure and temperature conditions spanning the entire range for Earth's lower mantle, 33–128 GPa and 1900–3000 K. Both in situ X-ray diffraction and ex situ transmission electron microscopy were used to determine synthesized phase assemblages and compositions of each phase. Experimental equations of state for bridgmanite can be used to determine composition within ~20 Fe# of the composition measured by EDX over a compositional range up to at least Fe#50. In all samples, magnesiowüstite composition was enriched in Fe relative to the starting material, demonstrating that Fe favors the oxide over the silicate phase throughout the lower mantle. In Fa72 samples, both EDX and XRD indicate that magnesiowüstite was within 5% Fe/(Mg + Fe) of pure FeO (i.e., Fe#95–100) between 50 and 100 GPa. Fe-content in bridgmanite increases with pressure up to ~80 GPa, reaching a maximum Fe# of 51 in Fa72 at 82 GPa. At 128 GPa, the Fe-content of the silicate phase is higher than that measured at lower pressures due to the higher silicate-oxide partitioning coefficient of Fe into post-perovskite relative to bridgmanite. The observations show no evidence of increase in partition coefficient due to a spin transition in bridgmanite. Decrease of the partition coefficient from 60 to 100 GPa in Fa72 is unlikely to be related to a spin transition in magnesiowüstite as the spin transition pressure in Fe#95–100 magnesiowüstite is greater than 100 GPa. Observed partitioning behaviors are successfully reproduced by self-consistent thermodynamic modeling with updated equation of state parameters for iron-rich bridgmanite and FeO. These results provide important constraints on the effect of Fe-content on partitioning of iron and resulting physical properties of iron-rich lower mantle heterogeneities. In iron-rich low shear velocity provinces, different effects of iron on densities of magnesiowüstite and bridgmanite result in increased effect of SiO_2-content to reduce the density of the bulk phase assemblage. Dynamics of iron-rich regions over Earth's history may have resulted in Si-depletion at the base of the mantle in LLSVPs and ULVZs.

Supplementary Materials: The following are available online at https://www.mdpi.com/article/10.3390/min11050512/s1. Figure S1: Mössbauer spectroscopy of a synthetic Fa50 olivine sample (A. Magrez, EPFL) demonstrates all iron adopts 2+ oxidation state, typical of synthetic [58] and natural olivine [59]. Figure S2: Scanning electron micrograph of thin section extracted by focused ion beam (FIB) from Fa45 sample heated to 2000 K at 40 GPa at APS GSECARS. Figure S3: Scanning electron micrograph of thin section extracted by focused ion beam (FIB) from Fa72 sample heated to 2000 K at 52 GPa at EPFL. Figure S4: Diffraction patterns for phase assemblages synthesized from Fa45 at 40–89 GPa. Bdg = bridgmanite, Mws = magnesiowüstite, N = NaCl medium. Reference stick pattern for Bdg is plotted below. For these experiments, λ = 0.3344 Å. Figure S5: Analytical TEM images of Mws grain in Fa72 sample heated to 2000 K at 82 GPa at EPFL. (a) STEM high-angle annular dark field (b) Energy-dispersive X-ray map with Mg, Fe, and Si concentrations coded in red, green, and blue respectively (c) Energy-dispersive X-ray map with O concentration coded in white. Figure S6: Analytical TEM images of Fa72 sample heated to 2000 K at 52 GPa at EPFL. (a) STEM high-angle annular dark field (b) Energy-dispersive X-ray map with Mg, Fe, and Si concentrations coded in red, green, and blue respectively (c) Energy-dispersive X-ray map with O concentration coded in white. Figure S7: TEM, STEM and EDX images of Fa45 sample heated to 2000 K at 40 GPa at APS GSECARS. (a) STEM bright field low magnification (b) STEM high-angle annular dark field low magnification (c) Energy-dispersive X-ray map with Mg, Fe, and Si concentrations coded in red, green, and blue respectively (d) TEM high magnification of sample center with euhedral grains (e) TEM high magnification of sample center showing disordered lattice planes in Mws grains and amorphized Bdg grains. Figure S8: (a) Lattice parameter *a* of bridgmanite at 300 K after laser heating with values from previously-measured 300 K compression of $(Mg,Fe)SiO_3$

bridgmanite [19,39,60]. Curves are fits to a linearized Birch-Murnaghan equation of state [61] with K_0' fixed at 4: $P = \frac{3}{2}K_0(X_{Fe})\left[\left(\frac{a_0(X_{Fe})}{a}\right)^7 - \left(\frac{a_0(X_{Fe})}{a}\right)^5\right]$, where P is pressure, X_{Fe} = Fe#, and a is the measured lattice parameter. The zero-pressure lattice parameter $a_0 = 4.787 + 0.123X_{Fe}$ and linear zero-pressure bulk modulus $K_0 = 212.2 + 8.5X_{Fe}$. (b) Difference between Fe# determined by the $P(a, X_{Fe})$ equation of state and Fe# of starting materials (standard deviation ~Fe#5). Figure S9: Unit cell volumes of ferropericlase—magnesiowüstite (Fp-Mws) phase at 300 K after quench of laser heated olivine samples with analogous measurements from San Carlos olivine composition by [38]. Open symbols are previously-measured 300 K volumes of (Mg,Fe)O [41,42,62,63]. Curves are fits to the Birch-Murnaghan equation of state [61]. Figure S10: Modeled pressure- and composition-dependence of partitioning behavior between bridgmanite and ferropericlase in olivine bulk compositions assuming ideal mixing (black curves) and nonideal mixing (for 10 in blue, 30 in green, 45 in orange, and 72% fayalite compositions in red). (a) models carried out using thermodynamic parameters for FeO as specified by [46], and (b) models carried out using updated thermodynamic parameters based on thermal equation of state of FeO by [42] and inversion of experimental partitioning data in this study, Figure S11: Densities at 300 K and selected lower mantle pressures 40, 60, 80, 100 and 125 GPa as a function of variable XFe = Fe/(Fe + Mg) for (a) bridgmanite [19,60] and post-perovskite [44,64,65] and (b) ferropericlase-magnesiowüstite [41,42,50,62,63,66–72]. Curves are linear or quadratic least-squares fits at each pressure. Table S1: Microprobe results for compositions of synthetic olivine starting materials, Table S2: Composition measurements and calculated partition coefficient obtained from energy-dispersive X-ray spectroscopic maps for each sample. Atomic percents of each element are averaged over pixels obtained from multiple grains. Bdg = bridgmanite, Mws = magnesiowüstite.

Author Contributions: Conceptualization, S.M.D., J.B. and and P.G.; Formal analysis, S.M.D. and C.-E.B., Funding acquisition, S.M.D. and P.G.; Investigation, S.M.D., F.N. and C.-E.B.; Methodology, S.M.D., V.B.P., M.C. and J.B.; Resources, V.B.P., M.C. and J.B.; Visualization, S.M.D.; Writing—original draft, S.M.D.; Writing—review and editing, S.M.D. and J.B. All authors have read and agreed to the published version of the manuscript.

Funding: GeoSoilEnviroCARS is supported by the National Science Foundation—Earth Sciences (EAR-0622171), Department of Energy—Geosciences (DE-FG02-94ER14466) and the State of Illinois. S. M. Dorfman acknowledges the Marie Heim-Vögtlin program of the Swiss National Science Foundation for financial support through project PMPDP2_151256 and National Science Foundation EAR-1664332. J. Badro acknowledges the financial support of the UnivEarthS Labex program at Sorbonne Paris Cité (ANR-10-LABX-0023 and ANR-11-IDEX-0005-02). J. Badro and Ch.-E. Boukaré acknowledge funding from the Swiss National Science Foundation through FNS Grants 200021_169854. Parts of this work were supported by IPGP multidisciplinary program PARI, and by Paris–IdF region SESAME Grant no. 12015908.

Data Availability Statement: Data are included in figures, tables and Supporting Information; additional original data are available upon request from dorfman3@msu.edu.

Acknowledgments: We thank R. Gaal for his major role in the design and construction of the EPFL laser heating system. N. Wehr assisted with synthesis of starting materials in piston-cylinder apparatus at IPGP. A. Magrez synthesized additional ^{57}Fe enriched olivine at EPFL. F. Bussy and R. Bodner of the University of Lausanne assisted with microprobe measurements of starting materials. F. Bobard, D. Alexander and E. Oveisi provided training and advice for focused ion beam and transmission electron microscopy.

Conflicts of Interest: The authors declare no conflict of interest. The funders had no role in the design of the study; in the collection, analyses, or interpretation of data; in the writing of the manuscript, or in the decision to publish the results.

Appendix A

Physical Properties of Iron-Rich Mantle Phases

Interpretation of in situ X-ray diffraction data and inferred physical properties of mantle phase assemblages require pressure-volume-composition equation of state data for bridgmanite (Bdg), ferropericlase–magnesiowüstite (Mws), and post-perovskite (pPv).

For quantitative analysis of Bdg composition at high pressures, recent compression measurements of single-phase Bdg with a wide range of Fe# synthesized in the laser-heated diamond anvil cell [19] were used to fit a pressure-lattice spacing-composition equation of state. The equation of state calibrates composition as a function of pressure and the *a* lattice parameter of bridgmanite, the direction most sensitive to Fe-content. For lattice parameter data from three studies of Fe-bearing Bdg by powder diffraction in quasi-hydrostatic media [19,39,60], compositions indicated by this calibration scatter around known compositions of starting materials with a standard deviation of ~5% (Supplementary Figure S7b). Note that data used for equation of state fits in these studies include only data obtained for Bdg observed without accessory SiO_2 or (Mg,Fe)O, and thus the compositions of the starting materials are assumed to be identical to the synthesized Bdg. Precision of composition estimates by XRD for this study and other typical partitioning studies will be lower due to the need to avoid internal pressure calibrants, which may complicate chemistry and/or result in Soret diffusion [35].

The composition of Mws is more difficult to model based on to unit cell volume than ferrous-iron-bearing Bdg due to the composition-dependent spin transition. For cubic Mws, unit cell volumes of B1-structure (Mg,Fe)O and B8 FeO were used to determine the pressure-volume-composition-spin state equation of state [41,42,50,62,63,66–73]. Magnesiowüstite with Fe# $\geq$ 95 may adopt the B8 structure at the pressure conditions of these experiments [74], but the diffraction peaks observed from this phase are not resolved well enough to determine its structure (Figure 1). Qualitatively, Mws volumes in Fa45 samples fall between previous measurements of Fe#58 and Fe#100 (FeO) compositions (Supplementary Figure S8). The measured volume of magnesiowüstite formed from Fa72 is consistent with nearly pure FeO.

These equation of state data for Bdg and Mws and composition-dependent equation of state of post-perovskite [44,64,65] were used to compute densities of mantle phases based on compositions set by partitioning constraints at model pressures of 40, 60, 80, 100, and 125 GPa. Mws pressure-volume-composition data were interpolated at each model pressure using quadratic trends (Supplementary Figure S9).

References

1. Deschamps, F.; Konishi, K.; Fuji, N.; Cobden, L. Radial thermo-chemical structure beneath Western and Northern Pacific from seismic waveform inversion. *Earth Planet. Sci. Lett.* **2019**, *520*, 153–163. [CrossRef]
2. Mao, W.L.; Shen, G.; Prakapenka, V.B.; Meng, Y.; Campbell, A.J.; Heinz, D.L.; Shu, J.; Hemley, R.J.; Mao, H.-K. Ferromagnesian postperovskite silicates in the D" layer of the Earth. *Proc. Natl. Acad. Sci. USA* **2004**, *101*, 15867–15869. [CrossRef]
3. Wicks, J.K.; Jackson, J.M.; Sturhahn, W. Very low sound velocities in iron-rich (Mg,Fe)O: Implications for the core-mantle boundary region. *Geophys. Res. Lett.* **2010**, *37*, L15304. [CrossRef]
4. Dorfman, S.M.; Duffy, T.S. Effect of Fe-enrichment on seismic properties of perovskite and post-perovskite in the deep lower mantle. *Geophys. J. Int.* **2014**, *197*, 910–919. [CrossRef]
5. Labrosse, S.; Hernlund, J.W.; Coltice, N. A crystallizing dense magma ocean at the base of the Earth's mantle. *Nature* **2007**, *450*, 866–869. [CrossRef] [PubMed]
6. Dobson, D.P.; Brodholt, J.P. Subducted banded iron formations as a source of ultralow-velocity zones at the core–mantle boundary. *Nature* **2005**, *434*, 371–374. [CrossRef]
7. Williams, Q.; Garnero, E.J. Seismic Evidence for Partial Melt at the Base of Earth's Mantle. *Science* **1996**, *273*, 1528–1530. [CrossRef]
8. Auzende, A.-L.; Badro, J.; Ryerson, F.J.; Weber, P.K.; Fallon, S.J.; Addad, A.; Siebert, J.; Fiquet, G. Element partitioning between magnesium silicate perovskite and ferropericlase: New insights into bulk lower-mantle geochemistry. *Earth Planet. Sci. Lett.* **2008**, *269*, 164–174. [CrossRef]
9. Irifune, T.; Shinmei, T.; McCammon, C.A.; Miyajima, N.; Rubie, D.C.; Frost, D.J. Iron Partitioning and Density Changes of Pyrolite in Earth's Lower Mantle. *Science* **2009**, *327*, 193–195. [CrossRef] [PubMed]
10. Nakajima, Y.; Frost, D.J.; Rubie, D.C. Ferrous iron partitioning between magnesium silicate perovskite and ferropericlase and the composition of perovskite in the Earth's lower mantle. *J. Geophys. Res. Solid Earth* **2012**, *117*, B08201. [CrossRef]
11. Sakai, T.; Ohtani, E.; Terasaki, H.; Miyahara, M.; Nishijima, M.; Hirao, N.; Ohishi, Y.; Sata, N. Fe–Mg partitioning between post-perovskite and ferropericlase in the lowermost mantle. *Phys. Chem. Miner.* **2010**, *37*, 487–496. [CrossRef]
12. Sakai, T.; Ohtani, E.; Terasaki, H.; Sawada, N.; Kobayashi, Y.; Miyahara, M.; Nishijima, M.; Hirao, N.; Ohishi, Y.; Kikegawa, T. Fe-Mg partitioning between perovskite and ferropericlase in the lower mantle. *Am. Miner.* **2009**, *94*, 921–925. [CrossRef]
13. Sinmyo, R.; Hirose, K.; Seto, Y.; Fujino, K.; Sata, N.; Ohishi, Y.; Nishio-Hamane, D. Partitioning of iron between perovskite/postperovskite and ferropericlase in the lower mantle. *J. Geophys. Res. Solid Earth* **2008**, *113*, 11. [CrossRef]

14. Sinmyo, R.; Hirose, K.; Muto, S.; Ohishi, Y.; Yasuhara, A. The valence state and partitioning of iron in the Earth's lowermost mantle. *J. Geophys. Res. Solid Earth* **2011**, *116*, B07205. [CrossRef]
15. Sinmyo, R.; Hirose, K. Iron partitioning in pyrolitic lower mantle. *Phys. Chem. Miner.* **2013**, *40*, 107–113. [CrossRef]
16. Muir, J.M.; Brodholt, J.P. Ferrous iron partitioning in the lower mantle. *Phys. Earth Planet. Inter.* **2016**, *257*, 12–17. [CrossRef]
17. Xu, S.; Lin, J.-F.; Morgan, D. Iron partitioning between ferropericlase and bridgmanite in the Earth's lower mantle. *J. Geophys. Res. Solid Earth* **2017**, *122*, 1074–1087. [CrossRef]
18. Piet, H.; Badro, J.; Nabiei, F.; Dennenwaldt, T.; Shim, S.-H.; Cantoni, M.; Hébert, C.; Gillet, P. Spin and valence dependence of iron partitioning in Earth's deep mantle. *Proc. Natl. Acad. Sci. USA* **2016**, *113*, 11127–11130. [CrossRef]
19. Dorfman, S.M.; Meng, Y.; Prakapenka, V.B.; Duffy, T.S. Effects of Fe-enrichment on the equation of state and stability of (Mg,Fe)SiO_3 perovskite. *Earth Planet. Sci. Lett.* **2013**, *361*, 249–257. [CrossRef]
20. Hsu, H.; Umemoto, K.; Blaha, P.; Wentzcovitch, R.M. Spin states and hyperfine interactions of iron in (Mg,Fe)SiO_3 perovskite under pressure. *Earth Planet. Sci. Lett.* **2010**, *294*, 19–26. [CrossRef]
21. Mao, Z.; Lin, J.-F.; Fu, S.; Okuchi, T.; Prakapenka, V.B.; Chow, P.; Wang, F.; Yang, J.; Wu, X.; Tomioka, N.; et al. Equation of state and hyperfine parameters of high-spin bridgmanite in the Earth's lower mantle by synchrotron X-ray diffraction and Mössbauer spectroscopy. *Am. Miner.* **2017**, *102*, 357–368. [CrossRef]
22. Dorfman, S.M.; Badro, J.; Rueff, J.-P.; Chow, P.; Xiao, Y.; Gillet, P. Composition dependence of spin transition in (Mg,Fe)SiO_3 bridgmanite. *Am. Miner.* **2015**, *100*, 2246–2253. [CrossRef]
23. Badro, J.; Fiquet, G.; Guyot, F.; Rueff, J.-P.; Struzhkin, V.V.; Vankó, G.; Monaco, G. Iron Partitioning in Earth's Mantle: Toward a Deep Lower Mantle Discontinuity. *Science* **2003**, *300*, 789–791. [CrossRef] [PubMed]
24. Badro, J.; Rueff, J.-P.; Vankó, G.; Monaco, G.; Fiquet, G.; Guyot, F. Electronic Transitions in Perovskite: Possible Nonconvecting Layers in the Lower Mantle. *Science* **2004**, *305*, 383–386. [CrossRef] [PubMed]
25. Lin, J.-F.; Speziale, S.; Mao, Z.; Marquardt, H. Effects of the Electronic Spin Transitions of Iron in Lower Mantle Minerals: Implications for Deep Mantle Geophysics and Geochemistry. *Rev. Geophys.* **2013**, *51*, 244–275. [CrossRef]
26. Badro, J. Spin Transitions in Mantle Minerals. *Annu. Rev. Earth Planet. Sci.* **2014**, *42*, 231–248. [CrossRef]
27. Caracas, R.; Ozawa, H.; Hirose, K.; Ishii, H.; Hiraoka, N.; Ohishi, Y.; Hirao, N. Identifying the spin transition in Fe^{2+}-rich $MgSiO_3$ perovskite from X-ray diffraction and vibrational spectroscopy. *Am. Miner.* **2014**, *99*, 1270–1276. [CrossRef]
28. Mao, W.L.; Meng, Y.; Shen, G.; Prakapenka, V.B.; Campbell, A.J.; Heinz, D.L.; Shu, J.; Caracas, R.; Cohen, R.E.; Fei, Y.; et al. Iron-rich silicates in the Earth's D″ layer. *Proc. Natl. Acad. Sci. USA* **2005**, *102*, 9751–9753. [CrossRef]
29. Tateno, S.; Hirose, K.; Sata, N.; Ohishi, Y. Solubility of FeO in (Mg,Fe)SiO_3 perovskite and the post-perovskite phase transition. *Phys. Earth Planet. Inter.* **2007**, *160*, 319–325. [CrossRef]
30. Hirose, K.; Takafuji, N.; Fujino, K.; Shieh, S.R.; Duffy, T.S. Iron partitioning between perovskite and post-perovskite: A transmission electron microscope study. *Am. Miner.* **2008**, *93*, 1678–1681. [CrossRef]
31. Akahama, Y.; Kawamura, H. Pressure calibration of diamond anvil Raman gauge to 310GPa. *J. Appl. Phys.* **2006**, *100*, 043516. [CrossRef]
32. Dorfman, S.M.; Prakapenka, V.B.; Meng, Y.; Duffy, T.S. Intercomparison of pressure standards (Au, Pt, Mo, MgO, NaCl and Ne) to 2.5 Mbar. *J. Geophys. Res. Solid Earth* **2012**, *117*, B08210. [CrossRef]
33. Prakapenka, V.B.; Kubo, A.; Kuznetsov, A.; Laskin, A.; Shkurikhin, O.; Dera, P.; Rivers, M.L.; Sutton, S.R. Advanced flat top laser heating system for high pressure research at GSECARS: Application to the melting behavior of germanium. *High Press. Res.* **2008**, *28*, 225–235. [CrossRef]
34. Carrez, P.; Leroux, H.; Cordier, P.; Guyot, F. Electron-irradiation-induced phase transformation and fractional volatilization in (Mg, Fe)$_2SiO_4$ olivine thin films. *Philos. Mag. A* **2001**, *81*, 2823–2840. [CrossRef]
35. Sinmyo, R.; Hirose, K. The Soret diffusion in laser-heated diamond-anvil cell. *Phys. Earth Planet. Inter.* **2010**, *180*, 172–178. [CrossRef]
36. Tange, Y.; Takahashi, E.; Nishihara, Y.; Funakoshi, K.-I.; Sata, N. Phase relations in the system MgO-FeO-SiO_2 to 50 GPa and 2000 °C: An application of experimental techniques using multianvil apparatus with sintered diamond anvils. *J. Geophys. Res. Solid Earth* **2009**, *114*, B02214. [CrossRef]
37. Frost, D.J.; Liebske, C.; Langenhorst, F.; McCammon, C.A.; Trønnes, R.G.; Rubie, D.C. Experimental evidence for the existence of iron-rich metal in the Earth's lower mantle. *Nature* **2004**, *428*, 409–412. [CrossRef] [PubMed]
38. Andrault, D. Evaluation of (Mg,Fe) partitioning between silicate perovskite and magnesiowustite up to 120 GPa and 2300 K. *J. Geophys. Res. Solid Earth* **2001**, *106*, 2079–2087. [CrossRef]
39. Mao, H.K.; Hemley, R.J.; Fei, Y.; Shu, J.F.; Chen, L.C.; Jephcoat, A.P.; Wu, Y.; Bassett, W.A. Effect of pressure, temperature, and composition on lattice parameters and density of (Fe,Mg)SiO_3-perovskites to 30 GPa. *J. Geophys. Res. Solid Earth* **1991**, *96*, 8069–8079. [CrossRef]
40. Speziale, S.; Milner, A.; Lee, V.E.; Clark, S.M.; Pasternak, M.P.; Jeanloz, R. Iron spin transition in Earth's mantle. *Proc. Natl. Acad. Sci. USA* **2005**, *102*, 17918–17922. [CrossRef]
41. Fei, Y.; Zhang, L.; Corgne, A.; Watson, H.; Ricolleau, A.; Meng, Y.; Prakapenka, V. Spin transition and equations of state of (Mg, Fe)O solid solutions. *Geophys. Res. Lett.* **2007**, *34*, 17307. [CrossRef]
42. Fischer, R.A.; Campbell, A.J.; Shofner, G.A.; Lord, O.T.; Dera, P.; Prakapenka, V.B. Equation of state and phase diagram of FeO. *Earth Planet. Sci. Lett.* **2011**, *304*, 496–502. [CrossRef]

43. Ozawa, H.; Hirose, K.; Ohta, K.; Ishii, H.; Hiraoka, N.; Ohishi, Y.; Seto, Y. Spin crossover, structural change, and metallization in NiAs-type FeO at high pressure. *Phys. Rev. B* **2011**, *84*, 134417. [CrossRef]
44. Zhang, L.; Meng, Y.; Mao, W.L. Effect of pressure and composition on lattice parameters and unit-cell volume of (Fe,Mg)SiO_3 post-perovskite. *Earth Planet. Sci. Lett.* **2012**, *317–318*, 120–125. [CrossRef]
45. Frost, D.J. Fe^{2+}-Mg partitioning between garnet, magnesiowüstite, and $(Mg,Fe)_2SiO_4$phases of the transition zone. *Am. Miner.* **2003**, *88*, 387–397. [CrossRef]
46. Stixrude, L.; Lithgow-Bertelloni, C. Thermodynamics of mantle minerals—II. Phase equilibria. *Geophys. J. Int.* **2011**, *184*, 1180–1213. [CrossRef]
47. Dorfman, S.M. Phase Diagrams and Thermodynamics of Lower Mantle Materials. In *Deep Earth: Physics and Chemistry of the Lower Mantle and Core*; Terasaki, H., Fischer, R.A., Eds.; John Wiley & Sons: Hoboken, NJ, USA, 2016; pp. 241–252.
48. Prescher, C.; Langenhorst, F.; Dubrovinsky, L.S.; Prakapenka, V.B.; Miyajima, N. The effect of Fe spin crossovers on its partitioning behavior and oxidation state in a pyrolitic Earth's lower mantle system. *Earth Planet. Sci. Lett.* **2014**, *399*, 86–91. [CrossRef]
49. Mao, H.-K.; Shen, G.; Hemley, R.J. Multivariable Dependence of Fe-Mg Partitioning in the Lower Mantle. *Science* **1997**, *278*, 2098–2100. [CrossRef]
50. Lin, J.-F.; Struzhkin, V.V.; Jacobsen, S.D.; Hu, M.Y.; Chow, P.; Kung, J.; Liu, H.; Mao, H.-K.; Hemley, R.J. Spin transition of iron in magnesiowüstite in the Earth's lower mantle. *Nature* **2005**, *436*, 377–380. [CrossRef]
51. Dorfman, S.M.; Potapkin, V.; Lv, M.; Greenberg, E.; Kupenko, I.; Chumakov, A.I.; Bi, W.; Alp, E.E.; Liu, J.; Magrez, A.; et al. Effects of composition and pressure on electronic states of iron in bridgmanite. *Am. Miner.* **2020**, *105*, 1030–1039. [CrossRef]
52. Bengtson, A.; Persson, K.; Morgan, D. Ab initio study of the composition dependence of the pressure-induced spin crossover in perovskite $(Mg_{1-x},Fe_x)SiO_3$. *Earth Planet. Sci. Lett.* **2008**, *265*, 535–545. [CrossRef]
53. Umemoto, K.; Wentzcovitch, R.M.; Yu, Y.G.; Requist, R. Spin Transition in $(Mg,Fe)SiO_3$ Perovskite under Pressure. *Earth Planet. Sci. Lett.* **2008**, *276*, 198–206. [CrossRef]
54. Catalli, K.; Shim, S.-H.; Prakapenka, V. Thickness and Clapeyron slope of the post-perovskite boundary. *Nature* **2009**, *462*, 782–785. [CrossRef]
55. Andrault, D.; Muñoz, M.; Bolfan-Casanova, N.; Guignot, N.; Perrillat, J.-P.; Aquilanti, G.; Pascarelli, S. Experimental evidence for perovskite and post-perovskite coexistence throughout the whole D″ region. *Earth Planet. Sci. Lett.* **2010**, *293*, 90–96. [CrossRef]
56. Deschamps, F.; Cobden, L.; Tackley, P.J. The primitive nature of large low shear-wave velocity provinces. *Earth Planet. Sci. Lett.* **2012**, *349–350*, 198–208. [CrossRef]
57. Catalli, K.; Shim, S.-H.; Prakapenka, V.B.; Zhao, J.; Sturhahn, W.; Chow, P.; Xiao, Y.; Liu, H.; Cynn, H.; Evans, W.J. Spin state of ferric iron in $MgSiO_3$ perovskite and its effect on elastic properties. *Earth Planet. Sci. Lett.* **2010**, *289*, 68–75. [CrossRef]
58. Dyar, M.D.; Sklute, E.C.; Menzies, O.N.; Bland, P.A.; Lindsley, D.; Glotch, T.; Lane, M.D.; Schaefer, M.W.; Wopenka, B.; Klima, R.; et al. Spectroscopic Characteristics of synthetic olivine: An integrated multi-wavelength and multi-technique approach. *Am. Mineral.* **2009**, *94*, 883–898. [CrossRef]
59. Dyar, M.D.; Agresti, D.G.; Schaefer, M.W.; Grant, C.A.; Sklute, E.C. Mössbauer spectroscopy of earth and planetary materials. *Annu. Rev. Earth Planet. Sci.* **2006**, *34*, 83–125. [CrossRef]
60. Lundin, S.; Catalli, K.; Santillán, J.; Shim, S.-H.; Prakapenka, V.; Kunz, M.; Meng, Y. Effect of Fe on the equation of state of mantle silicate perovskite over 1 Mbar. *Phys. Earth Planet. Inter.* **2008**, *168*, 97–102. [CrossRef]
61. Birch, F. Finite elastic strain of cubic crystals. *Phys. Rev.* **1947**, *71*, 809. [CrossRef]
62. Speziale, S.; Zha, C.-S.; Duffy, T.S.; Hemley, R.J.; Mao, H.-K. Quasi-hydrostatic compression of magnesium oxide to 52 GPa: Implications for the pressure-volume-temperature equation of state. *J. Geophys. Res. Solid Earth* **2001**, *106*, 515–528. [CrossRef]
63. Wicks, J.; Jackson, J.M.; Sturhahn, W.; Zhang, D. Sound velocity and density of magnesiowüstites: Implications for ultralow-velocity zone topography. *Geophys. Res. Lett.* **2017**, 2016GL071225. [CrossRef]
64. Guignot, N.; Andrault, D.; Morard, G.; Bolfancasanova, N.; Mezouar, M. Thermoelastic properties of post-perovskite phase $MgSiO_3$ determined experimentally at core–mantle boundary P–T conditions. *Earth Planet. Sci. Lett.* **2007**, *256*, 162–168. [CrossRef]
65. Nishio-Hamane, D.; Yagi, T. Equations of state for postperovskite phases in the $MgSiO_3$–$FeSiO_3$–$FeAlO_3$ system. *Phys. Earth Planet. Inter.* **2009**, *175*, 145–150. [CrossRef]
66. Chen, B.; Jackson, J.M.; Sturhahn, W.; Zhang, D.; Zhao, J.; Wicks, J.K.; Murphy, C.A. Spin crossover equation of state and sound velocities of $(Mg_{0.65}Fe_{0.35})O$ ferropericlase to 140 GPa. *J. Geophys. Res. Solid Earth* **2012**, *117*, B08208. [CrossRef]
67. Mao, Z.; Lin, J.-F.; Liu, J.; Prakapenka, V.B. Thermal equation of state of lower-mantle ferropericlase across the spin crossover. *Geophys. Res. Lett.* **2011**, *38*. [CrossRef]
68. Marquardt, H.; Speziale, S.; Reichmann, H.J.; Frost, D.J.; Schilling, F.R.; Garnero, E.J. Elastic Shear Anisotropy of Ferropericlase in Earth's Lower Mantle. *Science* **2009**, *324*, 224–226. [CrossRef]
69. Richet, P.; Mao, H.-K.; Bell, P.M. Bulk moduli of magnesiowüstites from static compression measurements. *J. Geophys. Res.* **1989**, *94*, 3037–3045. [CrossRef]
70. Solomatova, N.V.; Sturhahn, W.; Toellner, T.S.; Kalkan, B.; Steinhardt, W.M.; Jackson, J.M.; Wicks, J.K.; Zhao, J. Equation of state and spin crossover of (Mg,Fe)O at high pressure, with implications for explaining topographic relief at the core-mantle boundary. *Am. Miner.* **2016**, *101*, 1084–1093. [CrossRef]
71. Tange, Y.; Nishihara, Y.; Tsuchiya, T. Unified analyses for P-V-T equation of state of MgO: A solution for pressure-scale problems in high P-Texperiments. *J. Geophys. Res. Solid Earth* **2009**, *114*, B03208. [CrossRef]

72. ZhuravlevJ, K.K.; Jackson, J.M.; Wolf, A.S.; Wicks, J.K.; Yan, J.; Clark, S.M. Isothermal compression behavior of (Mg,Fe)O using neon as a pressure medium. *Phys. Chem. Miner.* **2010**, *37*, 465–474. [CrossRef]
73. Speziale, S.; Lee, V.E.; Clark, S.M.; Lin, J.F.; Pasternak, M.P.; Jeanloz, R. Effects of Fe spin transition on the elasticity of (Mg,Fe)O magnesiowüstites and implications for the seismological properties of the Earth's lower mantle. *J. Geophys. Res. Solid Earth* **2007**, *112*, B10212. [CrossRef]
74. Kondo, T.; Ohtani, E.; Hirao, N.; Yagi, T.; Kikegawa, T. Phase transitions of (Mg,Fe)O at megabar pressures. *Phys. Earth Planet. Inter.* **2004**, *143–144*, 201–213. [CrossRef]